remote sensing

MDPI

Article

Angle Estimation Based on Wave Path Difference Rate of Change Ambiguity Function

Jianye Xu [1,2], Maozhong Fu [3] and Zhenmiao Deng [1,2,*]

[1] School of Electronics and Communication Engineering, Shenzhen Campus, Sun Yat-sen University, Shenzhen 518107, China; xujy75@mail2.sysu.edu.cn
[2] School of Electronics and Communication Engineering, Sun Yat-sen University, Guangzhou 510275, China
[3] Fujian Key Laboratory of Communication Network and Information Processing, Xiamen University of Technology, Xiamen 361024, China; maozhongfu@gmail.com
* Correspondence: dengzhm7@mail.sysu.edu.cn

Abstract: Modern radar systems commonly utilize monopulse angle estimation techniques for target angle estimation, with the phase comparison method being one of the most widely adopted approaches. While the phase comparison method achieves high estimation precision, it is highly susceptible to noise and exhibits a suboptimal performance under low Signal-to-Noise Ratio (SNR) conditions, leading to a high SNR threshold. Moreover, conventional monopulse angle estimation methods provide limited target information, as a single measurement cannot reveal the target's motion direction. To address these shortcomings, a novel approach based on the phase comparison method is proposed in this study, with the variation in the wave path difference modeled as a first-order motion model. By accumulating the conjugate-multiplied signals over multiple time steps, the Wave Path Difference Rate of Change Ambiguity Function (WPD-ROC AF) is constructed. A fast algorithm employing the 2D Chirp-Z Transform (2D-CZT) is proposed, enabling multi-pulse angle estimation through the identification of frequency and phase values corresponding to spectral peaks. Simulation results validate that the proposed method outperforms traditional monopulse angle estimation techniques under low-SNR conditions and effectively suppresses static clutter interference. Furthermore, the sign of the WPD-ROC AF is shown to be correlated with the target's motion direction, providing practical utility for determining the direction of movement in remote sensing scenarios.

Keywords: angle estimation; phase comparison method; multi-pulse; WPD-ROC AF

check for updates

Academic Editor: Jingwei Xu

Received: 13 January 2025
Revised: 26 February 2025
Accepted: 3 March 2025
Published: 6 March 2025

Citation: Xu, J.; Fu, M.; Deng, Z. Angle Estimation Based on Wave Path Difference Rate of Change Ambiguity Function. *Remote Sens.* **2025**, *17*, 943. https://doi.org/10.3390/rs17050943

Copyright: © 2025 by the authors. Licensee MDPI, Basel, Switzerland. This article is an open access article distributed under the terms and conditions of the Creative Commons Attribution (CC BY) license (https://creativecommons.org/licenses/by/4.0/).

1. Introduction

The robust space surveillance system serves as a critical infrastructure for supporting military space applications, commercial space operations, and manned space missions in the context of remote sensing and space exploration [1–3]. Radar observations provide the means to precisely determine a target's spatial position, including the target's range, azimuth angle, and elevation angle [4]. However, high-precision estimations of range and velocity alone are insufficient for determining the target's position or orientation in space. Precise estimation of the target's azimuth and elevation angles from echo data is also necessary to enable comprehensive spatial determination, especially in remote sensing applications for tracking objects in space. In radar tracking applications, precise angle estimation plays a pivotal role in accurately determining the spatial position of a target [5].

Modern radar systems widely employ monopulse angle estimation techniques for measuring the angles of spatial targets [6–8]. In these systems, a radar simultaneously

transmits two identical beams from separate antennas and processes the amplitude [9–11] and phase [12–14] information in the received echo signals to estimate the target's angle. For instance, the widely used Amplitude Comparison Method (ACM) estimates the target's angle by analyzing the amplitude ratio of the echo signals from the two beams. Conversely, the phase comparison method (PCM) estimates the angle by leveraging the phase difference between the two beams' echo signals, which is then translated into a wave path difference to calculate the target's angle.

Monopulse angle estimation techniques have emerged as a focal point in angle estimation research due to their real-time processing capabilities and relatively low implementation complexity [15]. A significant challenge lies in applying monopulse angle estimation to multi-target scenarios [16]. When monopulse radar estimates the parameters of multiple targets, the output is limited to a single target set, and the estimation precision is heavily influenced by the phases, amplitudes, and other parameters of the multiple targets, leading to a marked reduction in precision [17]. To address this issue, the Asymptotic Maximum Likelihood Relaxed Estimation (AML-RELAX) method was proposed in [18,19], leveraging the Doppler frequency induced by target velocity to resolve individual targets and support the joint estimation of multiple parameters, including amplitude, angle, and velocity. Building on this, Fu et al. developed the Amplitude Comparison Monopulse–Maximum Likelihood (ACM-ML) algorithm [20], which employs joint estimations of range, velocity, and angle to accurately measure multiple targets within a single resolution cell. By transitioning traditional time domain signal processing to the frequency domain, this approach effectively mitigates range loss and distance migration issues. In wideband systems, additional challenges arise due to the energy dispersion of range-extended targets along the radial distance dimension. This restriction confines angle estimation to only the strong scattering centers of the target, resulting in Signal-to-Noise Ratio (SNR) degradation and poor angle estimation performance [21]. To address these difficulties, Zhang et al. proposed a method based on cross-correlation operations to accumulate the energy of different scatterers. This approach reformulates the angle estimation problem as a cross-correlation function (CCF) frequency estimation problem, significantly improving angle estimation performance [22]. Subsequently, Chen et al. introduced a minimum entropy phase estimation method to extract the phase of various scatterers and aggregate their energy, further improving angle estimation performance in wideband systems [23].

However, angle estimation demands stricter SNR conditions compared to the estimation of range and velocity. While the phase comparison method achieves high angle estimation precision, it is particularly sensitive to noise [24]. Consequently, the SNR threshold for phase comparison is higher than that of other angle estimation methods. Additionally, under low-SNR conditions, the use of a single pulse without energy accumulation causes the target to be obscured by noise and clutter, making it challenging to extract accurate amplitude and phase information. As a result, commonly used methods such as amplitude comparison and phase comparison struggle to estimate the target angle under these conditions. In other words, conventional monopulse angle estimation methods fail to maintain robust performance in low-SNR environments. Therefore, developing angle estimation algorithms capable of achieving high precision under low-SNR conditions has become a critical research focus.

Moreover, monopulse angle estimation provides only the target's angle at the current pulse time, without any information on how the angle changes during that pulse—specifically, the target's motion direction. To estimate the target's angular change, it is necessary to differentiate the angle estimation results from consecutive pulses to obtain the angular rate of change. However, this requires precise angle estimation, especially when the target is moving slowly, as the angular change between adjacent pulses becomes

less apparent. In such cases, any deviation in angle estimation could lead to misjudging the target's motion direction. Under low-SNR conditions, due to the degraded angle estimation performance, it becomes difficult to accurately capture the target's angular variation.

The aim of this study is to propose an angle estimation method that performs effectively under low-SNR conditions. The main contributions of this paper are as follows:

- In this study, to address the high SNR threshold and related challenges of the phase comparison monopulse angle estimation method, a Wave Path Difference Rate of Change Ambiguity Function (WPD-ROC-AF) is constructed by accumulating pulses during the Coherent Processing Interval (CPI). The frequency and phase corresponding to the spectral peaks are then estimated to obtain angle estimates, effectively shifting the SNR threshold and improving angle estimation precision.
- The spectral peaks of the WPD-ROC-AF are linked to the target's motion direction through their position along the rate of change dimension, allowing the determination of the target's motion trend based on their location.
- A maximum likelihood estimate of the angle based on the WPD-ROC-AF is presented, and its Cramér–Rao Lower Bound (CRLB) is derived. To reduce computational complexity, a fast algorithm based on the 2D-CZT is provided, enabling rapid and high-precision estimation of the target's angle.

This paper is organized as follows: Section 2 provides an analysis of the fundamental principles behind monopulse phase comparison angle estimation. Section 3 models the variation in wave path difference using a first-order motion model, derives the mathematical formulation for the proposed WPD-ROC AF-based angle estimation method, and discusses the CRLB for performance evaluation. Additionally, a fast algorithm based on the 2D-CZT is introduced to facilitate rapid and precise angle estimation. Section 4 presents simulation results comparing the proposed method with traditional phase comparison techniques, demonstrating significant improvements in estimation performance under low-SNR conditions. Furthermore, simulations with various moving target scenarios illustrate the method's capability to track target motion trends and provide precise angle estimates in static clutter environments. Finally, Section 5 provides a conclusion.

2. Phase Comparison Angle Estimation Method

2.1. Fundamental Principles

In phased array radars, the LFM echo signals are received, respectively, by four quadrants, which can be regarded as four identical antenna elements. These four signals will be coherently integrated to form four gain region signals S_{up}, S_{down}, S_{left}, and S_{right}. It is important to note that the radar system under consideration in this work is a ground-based phased array radar system. The schematic of the radar antenna array plane is shown in Figure 1.

Under the ideal far-field condition [25], the electromagnetic waves incident on the target can be approximated as plane waves. Consider quadrant A and quadrant B in the horizontal direction, where Figure 2 is the plane model of the phase comparison angle estimation method on the planar array antenna. Let the distance between the centers of the two quadrants be d and the angle between the target and the normal direction of the antenna array in the horizontal plane be θ. Due to the target's deviation from the normal direction of the phased array antenna plane, the echoes reflected from the target arrive at the two quadrants with different time delays. This results in a phase difference between the received echoes in quadrant A and quadrant B. By calculating the magnitude of this phase difference, the target's deviation from the normal direction of the antenna array plane can be determined, thereby enabling the estimation of the target's azimuth angle.

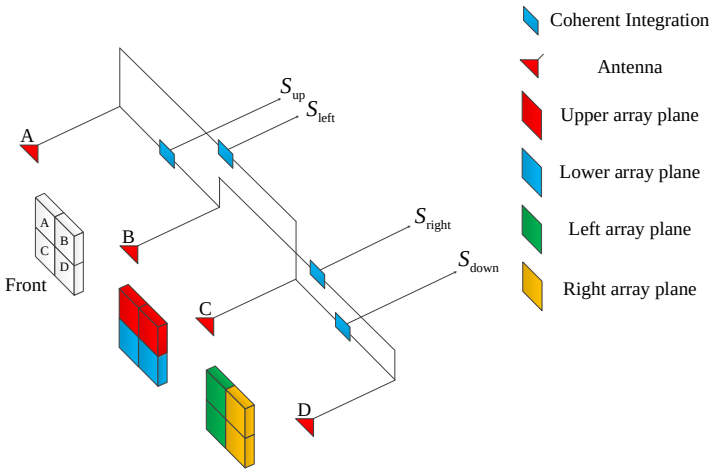


Figure 1. The schematic of the radar antenna array plane [22].

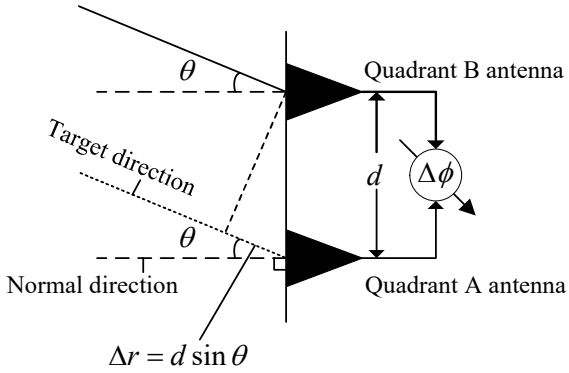


Figure 2. Phase comparison angle estimation method principle diagram.

The wave path difference between two received echo signals by the radar antenna can be expressed as follows:

$$\Delta r = d \sin\theta = \frac{c\Delta\varphi}{2\pi f_c} = \frac{\Delta\varphi}{2\pi}\lambda \tag{1}$$

The phase difference between the received echoes from different quadrants is induced by the wave path difference Δr, which can be explicitly expressed as follows:

$$\Delta\varphi = 2\pi\frac{\Delta r}{\lambda} = 2\pi\frac{d\sin\theta}{\lambda} \tag{2}$$

where λ represents the wavelength, and the angle θ can be calculated as

$$\theta = \arcsin\left(\frac{\lambda\Delta\varphi}{2\pi d}\right) \tag{3}$$

2.2. Signal Model

The radar echo after dechirp processing can be expressed as

$$\begin{aligned} s(\hat{t}, t_m) = {} & z \times \mathrm{rect}\left(\frac{\hat{t} - \frac{2R_\Delta}{c}}{T_p}\right) \\ & \times \exp\left(-j\frac{4\pi}{c}\gamma R_\Delta \hat{t}\right)\exp\left(-j\frac{4\pi}{c}f_c R_\Delta + j\frac{4\pi}{c^2}\gamma R_\Delta^2\right) + \tilde{u}(\hat{t}, t_m) \end{aligned} \tag{4}$$

where z represents the fluctuation of the received echo from the point target. $\tilde{u}(\hat{t}, t_m)$ denotes complex Gaussian noise with zero mean and variance $2\sigma^2$, $\hat{t}$ refers to fast time relative to the current pulse transmission time, $t_m = mT(m = 0, 1, 2, \ldots)$ represents the slow time, rect$(\cdot)$ is the rectangular window function, and T_p is the pulse duration. γ is the frequency modulation slope, and R_Δ is the distance difference between the target and the reference signal relative to the dechirped reference distance.

For convenience in representation and calculation, the received echoes from quadrant A and quadrant B can be expressed as follows based on the above formula:

$$\begin{aligned} s_1(t) &= \exp\left(-j2\pi\gamma\tau_{\Delta1}t - j2\pi f_c\tau_{\Delta1} + j\pi\gamma\tau_{\Delta1}^2\right) + u_1(t) \\ s_2(t) &= \exp\left(-j2\pi\gamma\tau_{\Delta2}t - j2\pi f_c\tau_{\Delta2} + j\pi\gamma\tau_{\Delta2}^2\right) + u_2(t) \end{aligned} \tag{5}$$

where $\tau_{\Delta1}$ and $\tau_{\Delta2}$ represent the relative time delays of the target's range gate leading edge in the received echoes from quadrant A and quadrant B, respectively, and $u_1(t)$ and $u_2(t)$ are the interference noise components in the received echoes from quadrant A and quadrant B, respectively. The expressions for $\tau_{\Delta1}$ and $\tau_{\Delta2}$ are as follows:

$$\begin{aligned} \tau_{\Delta1} &= \frac{2R_\Delta}{c} \\ \tau_{\Delta2} &= \frac{2R_\Delta - \Delta r}{c} \end{aligned} \tag{6}$$

To extract the phase difference between the two quadrants, the signals $s_1(t)$ and $s_2(t)$ in Equation (5) are mixed. The output signal obtained through conjugate multiplication is given by

$$\begin{aligned} s_{cm}(t) &= s_1(t)s_2^*(t) \\ &= \exp[-j2\pi\gamma(\tau_{\Delta1} - \tau_{\Delta2})t] \\ &\times \exp\left[-j2\pi f_c(\tau_{\Delta1} - \tau_{\Delta2}) + j\pi\gamma\left(\tau_{\Delta1}^2 - \tau_{\Delta2}^2\right)\right] + \tilde{u}(t) \\ &= s_{cm,s}(t) + \tilde{u}(t) \end{aligned} \tag{7}$$

The first term $s_{cm,s}(t)$ in the output of $s_{cm}(t)$ represents the desired signal, while the second term $\tilde{u}(t)$ corresponds to the accumulated noise component. To better illustrate the phase variation caused by the wave path difference, the term $s_{cm,s}(t)$ in Equation (7) can be rewritten as

$$s_{cm,s}(t) = \exp(-j2\pi\gamma\Delta\tau t - j\Delta\varphi) \tag{8}$$

where the time delay difference is $\Delta\tau = (\tau_{\Delta1} - \tau_{\Delta2})$, the phase difference is $\Delta\varphi = 2\pi f_c\Delta\tau - \pi\gamma(\tau_{\Delta1}^2 - \tau_{\Delta2}^2)$, and after compensating for the Residual Video Phase (RVP), the phase difference becomes $\Delta\varphi = 2\pi f_c\Delta\tau$.

Under the far-field condition, $s_{cm,s}(t)$ can be approximated as a single-frequency signal. Consequently, when the Discrete Fourier Transform (DFT) is applied to this signal, a spectral peak appears in the spectrum, with the corresponding frequency and phase given by

$$\begin{aligned} f' &= -\gamma\Delta\tau \\ \Delta\varphi &= 2\pi f_c\Delta\tau \end{aligned} \tag{9}$$

Thus, the wave path difference can be deduced from either the frequency or the phase corresponding to the spectral peak in the spectrum. The primary advantage of the phase comparison method is its high estimation precision; however, its major drawback lies in its sensitivity to environmental factors. Phase measurements are especially vulnerable to noise, leading to a poor angle estimation performance in low-SNR conditions. Consequently,

the SNR threshold for the phase comparison method is higher than that of other angle estimation methods.

2.3. The Impact of Target Angle on the Angle Estimation Precision

The core principle of the phase comparison method is to identify the primary spectral peak in the spectrum and estimate the angle using the phase associated with this peak. By rearranging Equation (2) and differentiating both sides, the following relationship is obtained:

$$\mathrm{d}\theta = \frac{\lambda}{2\pi d \cos\theta}\mathrm{d}\Delta\varphi \tag{10}$$

Based on the mathematical relationship expressed in Equation (10), it can be observed that the estimation of angle θ is nonlinearly influenced by the variation in phase difference $\Delta\varphi$. Specifically, the sensitivity of angle variation is proportional to the deviation from the normal direction. When $\theta = 0^\circ$, the target is aligned with the normal direction, and $\cos\theta$ reaches its maximum value of one, minimizing the term $\frac{\lambda}{2\pi d\cos\theta}$. As a result, a fixed phase difference $\mathrm{d}\Delta\varphi$ produces the minimal angle variation $\mathrm{d}\theta$, leading to the optimal estimation precision. As the angle θ deviates from the normal direction, the value of $\cos\theta$ decreases, causing the same phase difference $\mathrm{d}\Delta\varphi$ to produce a larger angle variation $\mathrm{d}\theta$, thereby reducing the estimation precision.

2.4. The Impact of Conjugate Multiplication Processing on the Angle Estimation Precision

In the phase comparison method, the phase difference between the echo signals received by two quadrants is typically extracted through conjugate multiplication operations. Specifically, conjugate multiplication of the echo signals from two quadrants yields a cross-correlation signal containing phase difference information. By analyzing the phase characteristics of this signal, the angular deviation of the target can be determined. However, this conjugate multiplication process inevitably generates signal noise cross-product terms, which degrade the output signal quality. This phenomenon results in a significantly lower SNR of the cross-correlation signal compared to that of the original received signals, thereby inducing SNR degradation. To quantitatively evaluate the impact of this processing method on system performance, this subsection analyzes the SNR attenuation level caused by conjugate multiplication under different deskewed echo SNR conditions.

Let $s(t)$ be the dechirped echo with amplitude A and $u(t)$ be the additive noise in the echo following zero-mean Gaussian white noise of variance σ^2. The echo signals from the two quadrants can then be expressed as

$$\begin{aligned} x_1(t) &= s_1(t) + u_1(t) \\ x_2(t) &= s_2(t) + u_2(t) \end{aligned} \tag{11}$$

For $x_1(t)$ and $x_2(t)$, the SNR is defined as

$$\mathrm{SNR} = \frac{A^2}{\sigma^2} \tag{12}$$

From Equation (7), the conjugate multiplication processing result of $x_1(t)$ and $x_2(t)$ can be expressed as

$$\begin{aligned} x_{cm}(t) &= x_1(t)x_2^*(t) \\ &= s_1(t)s_2^*(t) + s_1(t)u_2^*(t) + u_1(t)s_2^*(t) + u_1(t)u_2^*(t) \\ &= x_s(t) + x_c(t) + x_u(t) \end{aligned} \tag{13}$$

where $x_s(t)$ represents the desired signal component, $x_c(t)$ denotes the cross-term between the signal and noise, and $x_u(t)$ corresponds to the accumulated noise term. Both the signal noise cross-term and the accumulated noise term are regarded as noise components independent of the signal, which are undesirable in our analysis.

Based on Equation (13), the power of the desired signal term $x_s(t)$ can be calculated as A^4, and the power of the noise term $x_c(t) + x_u(t)$ is $2A^2\sigma^2 + \sigma^4$. Therefore, the SNR of the conjugate cross-correlation signal can be defined as

$$\mathrm{SNR}_{cm} = \frac{A^4}{2A^2\sigma^2 + \sigma^4} \tag{14}$$

Based on the original signal SNR described by Equation (12) and the post-processed SNR after the conjugate cross-correlation operation specified in Equation (14), we conducted numerical simulations to generate comparative SNR curves before and after the conjugate multiplication processing. Furthermore, we quantitatively analyzed the relationship between SNR loss and the original input SNR, with the simulation results presented in Figure 3. From Figure 3a, it is clear that the SNR of the echoes after conjugate multiplication is significantly lower than that of the original dechirped echoes, indicating a noticeable loss. Figure 3b shows that the SNR loss due to conjugate multiplication decreases as the original echo SNR increases. However, as the original echo SNR continues to rise, the SNR loss approaches approximately 3 dB and then stabilizes. Therefore, in low-SNR environments, the monopulse phase comparison method, which does not involve energy accumulation, experiences a significant SNR loss due to conjugate multiplication, primarily because of the low SNR in the original signal. This is one of the reasons why the phase comparison method requires a higher SNR threshold.

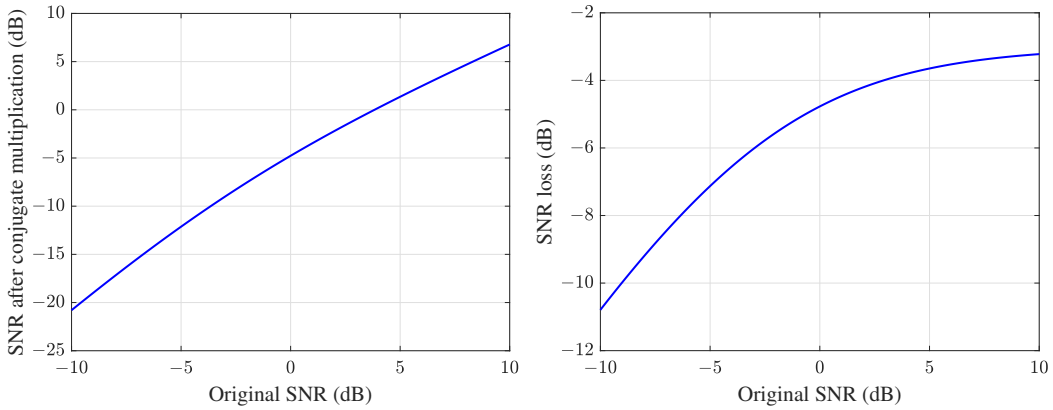


Figure 3. The impact of conjugate multiplication on SNR. (**a**) The relationship between the SNR before and after conjugate multiplication; (**b**) the relationship between SNR loss and the original input SNR.

3. Angle Estimation Based on WPD-ROC AF

As discussed in the previous section, the phase comparison monopulse method is sensitive to noise, and the conjugate multiplication operation it employs results in an SNR loss. As a result, the traditional phase comparison monopulse method has a higher SNR threshold and performs poorly in low-SNR environments. Additionally, this method only provides the target's angle at the current moment. To track the target's angular variation and motion direction, it is necessary to differentiate the angle estimates from adjacent pulses to obtain the rate of angle change. However, this requires precise angle estimation,

which is particularly challenging in low-SNR conditions due to the poor performance of angle estimation, which makes it difficult to accurately track changes in the target's angle.

In response to the challenges of the traditional monopulse phase comparison method, a novel approach based on the WPD-ROC-AF is introduced in this study. By accumulating multiple pulses, this method enhances the SNR and substantially improves the angle estimation performance, particularly in low-SNR environments.

3.1. The First-Order Motion Model of the Target's Wave Path Difference

As the target moves, both the angle of deviation from the normal direction of the array and the wave path difference between the receiving array will change. As shown in Equation (1), the variation in the wave path difference Δr can be used to derive the change in angle. Assuming a stop-and-go model, the wave path difference at each pulse time is expressed as follows:

$$\Delta r_m \approx \Delta r_0 + v_{\Delta r} t_m = \Delta r_0 + v_{\Delta r} \times (mT) \tag{15}$$

where $m \in [-M, M]$ is the pulse index in the slow-time dimension, $2M + 1$ is the total number of pulses, $t_m = mT$ represents the time corresponding to each pulse, Δr_0 is the wave path difference at the initial time, and $v_{\Delta r}$ represents the rate of change of the target's wave path difference.

Equation (15) approximates the change in the target's wave path difference across pulses using a first-order motion model. Combined with Equation (1), this enables the determination of the target's angular variation over each pulse.

3.2. WPD-ROC AF

Under the assumption of a fixed target motion model, the common approach is to use observed data to determine the optimal parameter values that maximize the likelihood, forming the basis of Maximum Likelihood Estimation (MLE) [26]. Based on the actual radar echo model, if the motion characteristics of the spatial target are known, the most likely motion characteristics of the target can be deduced by maximizing the statistical probability using the known observation samples. Next, based on the first-order motion model of the target's wave path difference, we derive the WPD-ROC AF.

Assuming the target satisfies the far-field conditions, based on Equations (7) and (8), the conjugate cross-correlation signal obtained by conjugate multiplication of the two received quadrant echoes can be approximated as

$$x(t) = z \exp(-j2\pi\gamma\Delta\tau t - j2\pi f_c \Delta\tau) + u(t) \tag{16}$$

where $u(t)$ represents the cross-term and noise.

By combining Equation (15), Equation (16) can be rewritten in the form of a state estimate for wave path difference as the state variable:

$$x_{m,n} = z \exp\left(-j\frac{2\pi}{c}\Delta r_m(\gamma n\Delta t + f_c)\right) + u(n) \tag{17}$$

where $n \in [-N/2, N/2 - 1]$ represents the index of the fast time dimension sample points, N denotes the number of sample points per pulse, and $\Delta t = 1/f_s$ is the time interval between the fast time sample points.

To achieve a high-precision estimation of the wave path difference, conjugate cross-correlation signals formed from multiple reception moments are accumulated. This accumulation enhances the SNR, thereby improving the wave path difference estimation precision and lowering the SNR threshold. Through this accumulation, the WPD-ROC

AF is constructed. Assuming that the noise $u(n)$ in Equation (17) follows a zero-mean Gaussian white noise distribution with variance σ^2, the joint probability density function of its real and imaginary parts is given by

$$p(u(n)|\Delta r, v_{\Delta r}) = \frac{1}{(\pi\sigma^2)^{(N)(2M+1)}} \times \exp\left\{ -\frac{\sum_{m,n} \left| x_{m,n} - z\exp\left[-j\frac{2\pi}{c}\Delta\hat{r}_m(\Delta r, v_{\Delta r})(\gamma n\Delta t + f_c)\right]\right|^2}{\sigma^2} \right\} \tag{18}$$

The likelihood function is equivalent to the inverse of the conditional probability density function. After eliminating the coefficient in front of the likelihood function and taking the logarithm, the likelihood function can be equivalently expressed as

$$L(\Delta r, v_{\Delta r}) = -\sum_{m,n} \left| x_{m,n} - z\exp\left[-j\frac{2\pi}{c}\Delta\hat{r}_m(\Delta r, v_{\Delta r})(\gamma n\Delta t + f_c)\right]\right|^2 \tag{19}$$

It can be observed that the value of this function is determined by parameters Δr and $v_{\Delta r}$. When these two parameters maximize the likelihood function, their corresponding values represent the estimated parameters. Therefore, the two-dimensional likelihood function formed after accumulating the conjugate cross-correlation signals from multiple reception moments is defined as

$$H(\Delta r, v_{\Delta r}) = \left| \sum_{m,n} x_{m,n}\exp\left[j\frac{2\pi}{c}\Delta\hat{r}_m(\Delta r, v_{\Delta r})(\gamma n\Delta t + f_c)\right]\right| \tag{20}$$

The estimated values of the initial wave path difference and its rate of change satisfy the following condition:

$$(\Delta\hat{r}_0, \hat{v}_{\Delta r}) = \arg\left(\max_{\Delta r, v_{\Delta r}} H(\Delta r, v_{\Delta r})\right) \tag{21}$$

Equations (20) and (21) indicate that the peak in the WPD-ROC AF must be located. The frequency corresponding to this peak, along with the phase of the two-dimensional spectral peak, can be used to estimate the initial wave path difference at the starting moment $\Delta\hat{r}_0$. Furthermore, the Doppler frequency associated with the peak provides the estimation of the rate of change of the wave path difference $\hat{v}_{\Delta r}$.

Figure 4 shows the spectrum of the conjugate cross-correlation signal for eight consecutive pulses, while Figure 5 presents the WPD-ROC AF obtained through the accumulation of these eight pulses. A comparison reveals that the two-dimensional spectrum resulting from multi-pulse accumulation exhibits a significantly higher SNR, thereby enabling more accurate identification of the frequency and phase values.

3.3. Cramér–Rao Lower Bound

According to estimation theory, when estimating the value of an unknown parameter θ in the presence of noise, if the mathematical expectation of the estimator equals the true value of the parameter, the estimator is considered unbiased [27]. Otherwise, it is biased. The CRLB provides a lower bound on the Mean Square Error (MSE) of any unbiased estimator [28], meaning that it is impossible to achieve an MSE smaller than this lower bound for an unbiased estimator. The CRLB serves as a benchmark for evaluating the performance of unbiased estimators. The MLE used in this study is an asymptotically unbi-

ased estimator, and when the sample size is sufficiently large, its performance approaches that of an unbiased estimator.

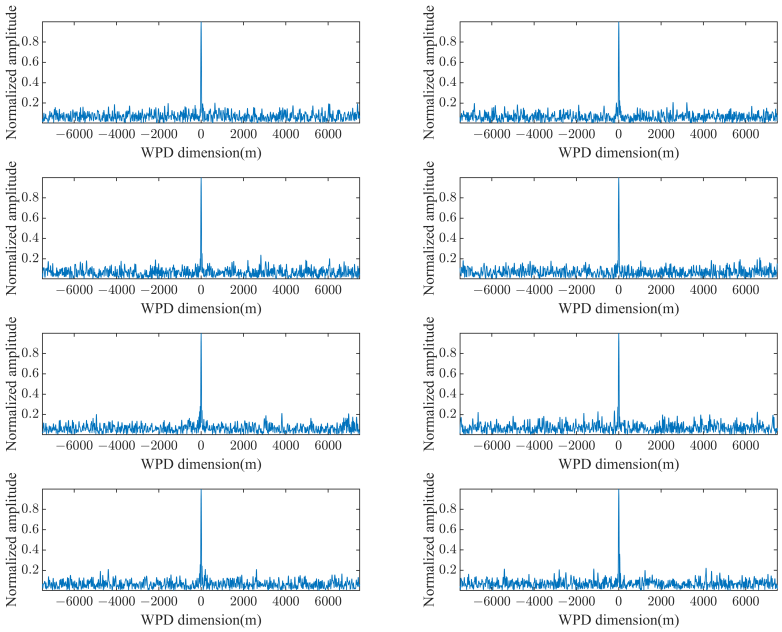
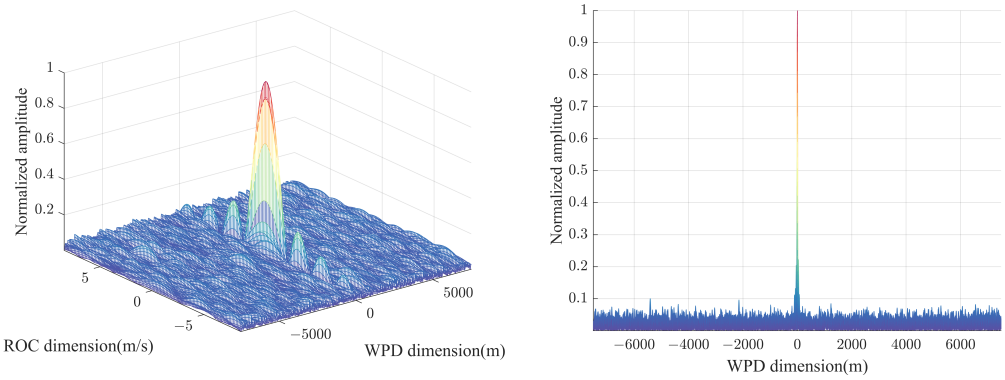


Figure 4. The spectrum of the conjugate cross-correlation signal at eight consecutive time instances.



(**a**) (**b**)

Figure 5. The WPD-ROC AF obtained by accumulating eight conjugate cross-correlation signals. (**a**) WPD-ROC AF; (**b**) the cross-sectional plot of WPD-ROC AF.

As shown in the previous section, the likelihood function can be defined as follows:

$$\begin{aligned} F(\Delta r, v_\Delta) &= -\frac{1}{\sigma^2}|x_{m,n} - d_{m,n}|^2 \\ &= -\frac{1}{\sigma^2}(x_{m,n} - d_{m,n})(x_{m,n} - d_{m,n})^* \end{aligned} \tag{22}$$

where

$$d_{m,n} = z \exp\left[-j\frac{2\pi}{c}\Delta\hat{r}_m(\Delta r + v_{\Delta r}t_m)(\gamma n\Delta t + f_c)\right] \tag{23}$$

The corresponding elements of the Fisher information matrix can be obtained as follows:

$$\begin{aligned} J_{\Delta r,\Delta r} &= -\mathrm{E}\left\{\frac{\partial^2 F}{\partial \Delta r^2}\right\} \\ &= -\frac{1}{\sigma^2}\sum_{m,n}\mathrm{E}\{\mathrm{Re}(K_1)\} \end{aligned} \tag{24}$$

where

$$K_1 = \frac{\partial^2 d_{m,n}}{\partial \Delta r^2}(x_{m,n} - d_{m,n})^* - 2\frac{\partial d_{m,n}}{\partial \Delta r}\frac{\partial d_{m,n}^*}{\partial \Delta r} + \frac{\partial^2 d_{m,n}^*}{\partial \Delta r^2}(x_{m,n} - d_{m,n}) \tag{25}$$

It can be deduced that

$$\begin{aligned} J_{\Delta r,\Delta r} &= -\mathrm{E}\left\{\frac{\partial^2 F}{\partial \Delta r^2}\right\} \\ &= \frac{2}{\sigma^2}\sum_{m,n}\mathrm{E}\left\{\mathrm{Re}\left(\frac{\partial d_{m,n}}{\partial \Delta r}\frac{\partial d_{m,n}^*}{\partial \Delta r}\right)\right\} \\ &= \frac{32\pi z^2}{c^2\sigma^2}\sum_{m,n} L_1^2 \end{aligned} \tag{26}$$

The same can be obtained:

$$\begin{aligned} J_{\Delta r,v_{\Delta r}} = J_{v_{\Delta r},\Delta r} &= -\mathrm{E}\left\{\frac{\partial^2 F}{\partial \Delta r \partial v_{\Delta r}}\right\} \\ &= \frac{1}{\sigma^2}\sum_{m,n}\mathrm{E}\left\{\mathrm{Re}\left(\frac{\partial d_{m,n}}{\partial \Delta r}\frac{\partial d_{m,n}^*}{\partial v_{\Delta r}} + \frac{\partial d_{m,n}}{\partial v_{\Delta r}}\frac{\partial d_{m,n}^*}{\partial \Delta r}\right)\right\} \\ &= \frac{32\pi z^2}{c^2\sigma^2}\sum_{m,n} L_1 L_2 \end{aligned} \tag{27}$$

$$\begin{aligned} J_{v_{\Delta r},v_{\Delta r}} &= -\mathrm{E}\left\{\frac{\partial^2 F}{\partial {v_{\Delta r}}^2}\right\} \\ &= \frac{2}{\sigma^2}\sum_{m,n}\mathrm{E}\left\{\mathrm{Re}\left(\frac{\partial d_{m,n}}{\partial v_{\Delta r}}\frac{\partial d_{m,n}^*}{\partial v_{\Delta r}}\right)\right\} \\ &= \frac{32\pi z^2}{c^2\sigma^2}\sum_{m,n} L_2^2 \end{aligned} \tag{28}$$

where

$$L_1 = \gamma n \Delta t + f_c \tag{29}$$

$$L_2 = (\gamma n \Delta t + f_c)t_m = (\gamma n \Delta t + f_c)mT \tag{30}$$

Thus, the Fisher information matrix $\mathbf{I}$ for the wave path difference Δr and the rate of change of the wave path difference $v_{\Delta r}$ can be expressed as

$$\mathbf{I} = \begin{bmatrix} J_{\Delta r,\Delta r} & J_{v_{\Delta r,}\Delta r} \\ J_{\Delta r,v_{\Delta r}} & J_{v_{\Delta r},v_{\Delta r}} \end{bmatrix} \tag{31}$$

By inverting the Fisher information matrix $\mathbf{I}$, the CRLB matrix $\mathbf{C}$ can be obtained

$$\mathbf{C} = \mathbf{I}^{-1} \tag{32}$$

Extracting the diagonal elements of the matrix, the CRLB for Δr and $v_{\Delta r}$ are given as follows:

$$\begin{aligned} \mathrm{E}\{(\Delta r - \Delta r_0)\} &= \frac{J_{v_{\Delta r},v_{\Delta r}}}{J_{\Delta r,\Delta r}J_{v_{\Delta r},v_{\Delta r}} - J_{v_{\Delta r},\Delta r}J_{\Delta r,v_{\Delta r}}} \\ &= \frac{c^2\sigma^2}{32\pi z}\frac{\sum_{m,n} L_2^2}{\sum_{m,n} L_1^2 \sum_{m,n} L_2^2 - \sum_{m,n}(L_1 L_2)^2} \end{aligned} \tag{33}$$

$$\begin{aligned} \mathrm{E}\{(v_{\Delta r} - v_{\Delta r_0})\} &= \frac{J_{\Delta r,\Delta r}}{J_{\Delta r,\Delta r} J_{v_{\Delta r},v_{\Delta r}} - J_{v_{\Delta r},\Delta r} J_{\Delta r,v_{\Delta r}}} \\ &= \frac{c^2\sigma^2}{32\pi z} \frac{\sum_{m,n} L_1^2}{\sum_{m,n} L_1^2 \sum_{m,n} L_2^2 - \sum_{m,n} (L_1 L_2)^2} \end{aligned} \tag{34}$$

By substituting Equations (29) and (30), it can be derived that

$$\mathrm{E}\{(\Delta r - \Delta r_0)\} = \frac{c^2\sigma^2}{32\pi z} \frac{\sum_m (mT)^2}{\sum_n (\gamma n \Delta t + f_c)^2 \sum_m (mT)^2 - \sum_m (mT)} \tag{35}$$

$$\mathrm{E}\{(v_{\Delta r} - v_{\Delta r_0})\} = \frac{c^2\sigma^2}{32\pi z} \frac{1}{\sum_n (\gamma n \Delta t + f_c)^2 \sum_m (mT)^2 - \sum_m (mT)} \tag{36}$$

3.4. The 2D-CZT-Based Fast Angle Estimation Algorithm

The data matrix expressed in Equation (20) requires performing a global search in the WPD-ROC AF plane, which results in high computational complexity. To mitigate this, efficient algorithms must be employed. Since the explicit form of Equation (20) represents a two-dimensional sine wave, the Two-Dimensional Fast Fourier Transform (2D-FFT) [29], based on complex sinusoidal signals, can be used for computation. While the 2D-FFT has been optimized for accelerated computation, zero padding is applied in practical estimation to improve the search accuracy. However, this increases both memory usage and computation time. Therefore, the aim is to improve estimation efficiency while preserving high search accuracy.

To illustrate the distribution of targets in the ambiguity function, simulations are conducted for a single moving target, with the radar system parameters summarized in Table 1.

Table 1. Parameters of radar system.

Symbol	Parameters	Value
f_c	Carrier frequency	8.75 GHz
BW	Bandwidth	5 MHz
PW	Pulse width	100 μs
PRF	Pulse repetition frequency	1000 Hz
f_s	Sampling frequency	5 MHz
NP	Number of pulses	32
d	Quadrant array spacing	5 m

The spectrum of the WPD-ROC AF obtained using the 2D-FFT is shown in Figure 6. Upon inspection, it is evident that not all frequencies are relevant as regions corresponding to frequencies outside the target's location are of no interest. Since our study focuses on a single-target scenario, the search is concentrated around the main spectral peak. Therefore, a Fourier transform is first applied for rough estimation to determine the target's frequency range. Following this, the Chirp-Z Transform (CZT) [30] is employed to perform the Discrete Fourier Transform (DFT) [31] within the specific frequency range of interest.

By using the 2D-FFT for a rough estimation strategy, the focus is placed on specific frequency ranges of interest. The WPD-ROC AF obtained using the 2D-CZT is shown in Figure 7. From the spectrum, it can be observed that the search is concentrated within a smaller range, enabling a more refined search. Compared to the 2D-FFT, the 2D-CZT not only achieves a higher search accuracy but also effectively reduces the computational complexity. Therefore, in this paper, the 2D-CZT is integrated to perform the search on the WPD-ROC AF, enabling fast angle estimation.

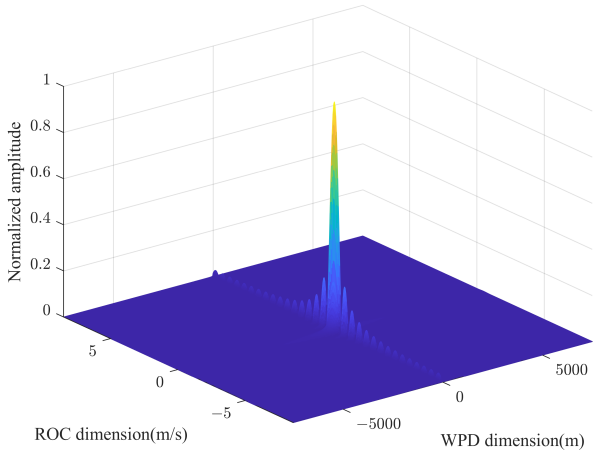


Figure 6. 2D-FFT spectrum.

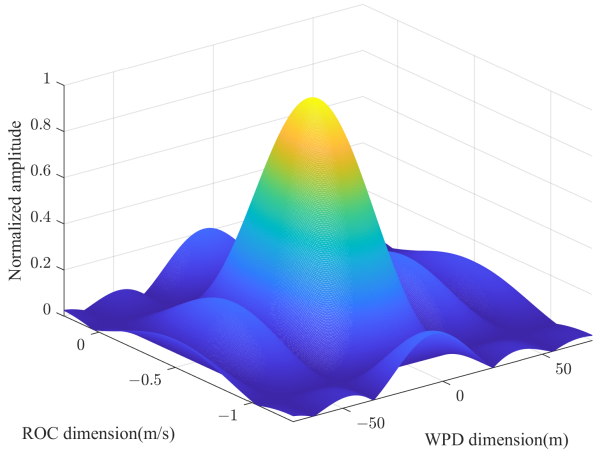


Figure 7. 2D-CZT spectrum.

3.5. Denoising of WPD-ROC AF

Due to the short duration of a single frame, it can be assumed that the target's velocity remains nearly constant during that time. A Fourier transform in the Doppler domain is applied to the echo signal of a single target in one quadrant. Under high SNR conditions, as shown in Figure 8a, the peak is concentrated at a specific position in the Doppler domain, with other positions representing noise. However, under low-SNR conditions, as shown in Figure 8b, the target's spectral peak is submerged in noise. This occurs because energy accumulation is only performed in the Doppler domain. By performing a two-dimensional Fourier transform on the echo signal to further accumulate energy, as shown in Figure 8c, the target's spectral peak becomes much more distinct. It is important to note that the low-SNR conditions in Figure 8b,c are based on the same SNR values to ensure consistency in the analysis.

To address this phenomenon, a novel denoising method is proposed. The echo signals from the two quadrants are individually subjected to a two-dimensional Fourier transform to identify the location of the target spectral peak in the Doppler dimension for each signal. Based on the positions of the spectral peak in the Doppler dimension, a filter is then applied in the slow-time dimension to perform denoising. This approach enhances the detection performance, particularly under low-SNR conditions. The effectiveness of the proposed denoising method is demonstrated in Figure 9. The low-SNR conditions in Figure 9 are the

same as those in Figure 8 to ensure a consistent comparison across the results. Figure 9a shows the WPD-ROC AF obtained from the cross-correlation of the echo signals without denoising, where no distinct target is visible. Figure 9b shows the WPD-ROC AF after denoising, where a clear spectral peak is observed.

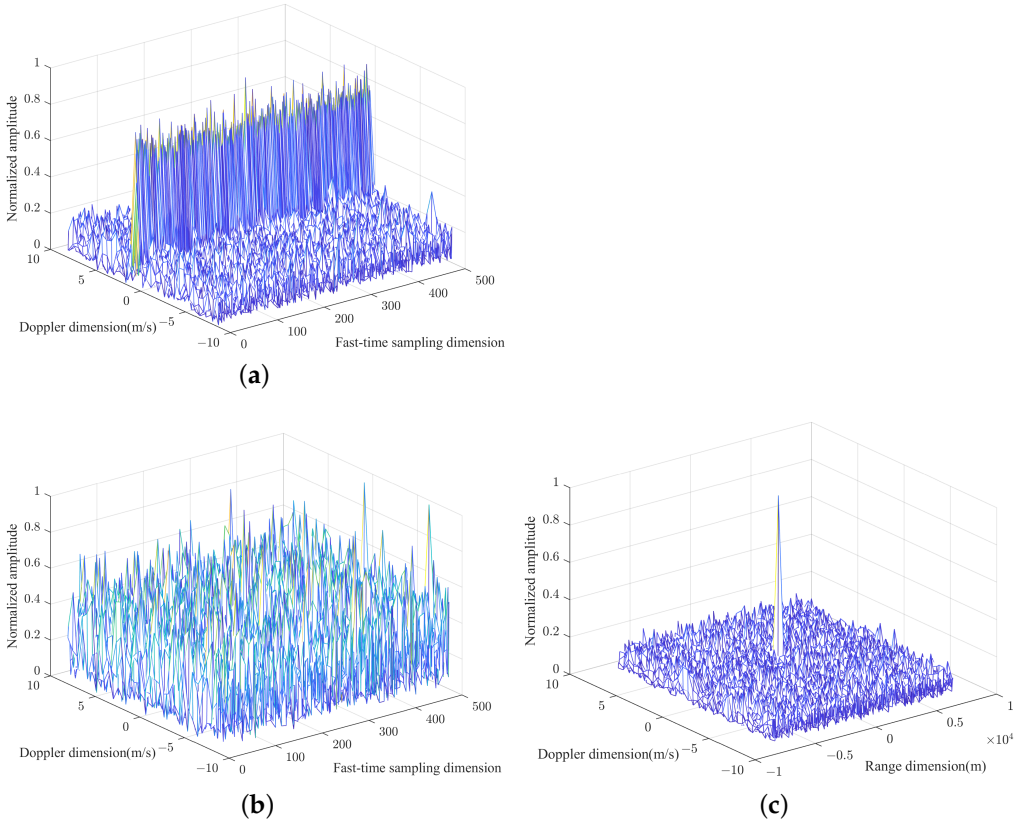


Figure 8. Comparison of spectrum at high and low SNR. (**a**) Doppler transform spectrum at high SNR; (**b**) Doppler transform spectrum at low SNR; (**c**) two-dimensional transform spectrum at low SNR.

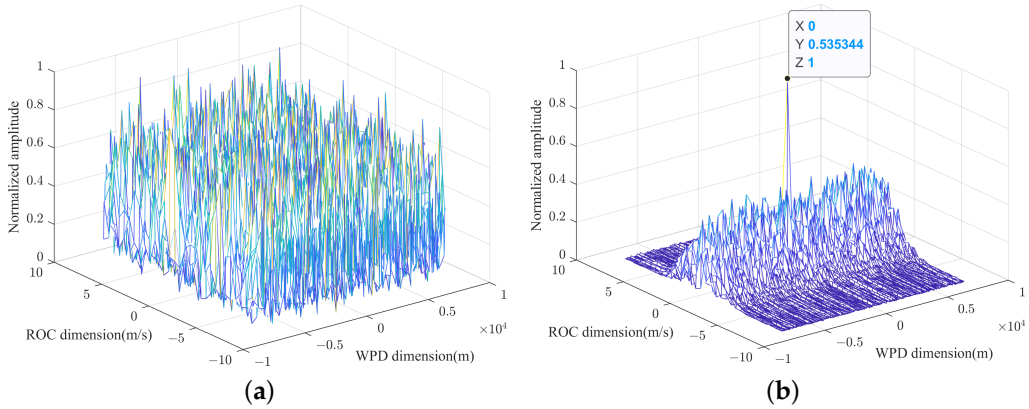


Figure 9. Comparison of WPD-ROC AF with and without denoising. (**a**) WPD-ROC AF without denoising; (**b**) denoised WPD-ROC AF.

To further validate the effectiveness of the denoising process, a Monte Carlo simulation was conducted. The radar parameters are set as shown in Table 1, with 1000 simulation runs. As shown in Figure 10, the denoising method significantly lowers the SNR threshold for angle estimation compared to the method without denoising.

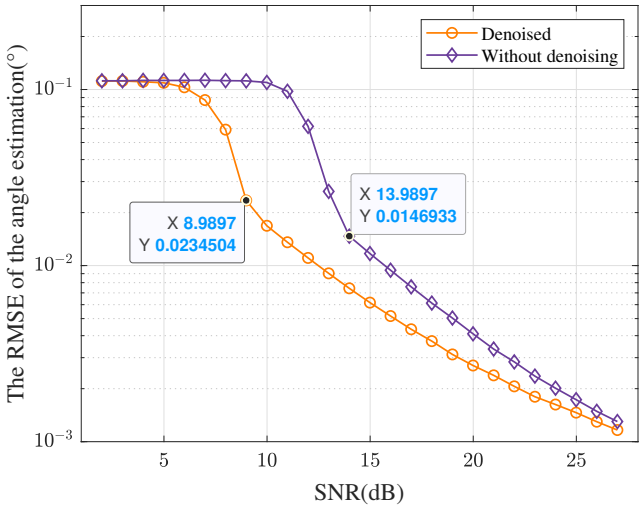


Figure 10. Comparison of angle estimation precision with and without denoising.

3.6. Joint Angle Estimation Algorithm

Building on the analysis in this section, a joint angle estimation algorithm based on the WPD-ROC AF is proposed in this study, which delivers a robust angle estimation performance in low-SNR environments while ensuring high computational efficiency.

The algorithm can be summarized as follows: First, for the signals from two quadrants, noise reduction is applied to the signals from the two quadrants using filters based on the peak positions of the range–velocity ambiguity function. Once denoising is complete, the cross-correlation operation is performed to obtain the WPD-ROC AF. Next, a coarse estimation algorithm is employed to obtain low-precision estimates of the wave path difference and rate of change. Finally, a fast 2D-CZT-based algorithm is used to refine the spectral peak search, resulting in high-precision estimates for both the wave path difference and rate of change. The flowchart of the proposed joint angle estimation algorithm is shown in Figure 11.

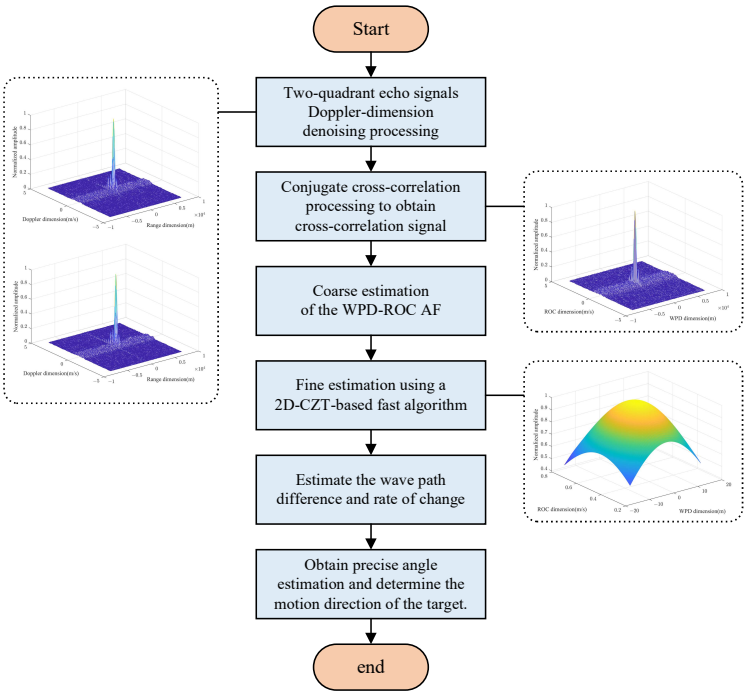


Figure 11. Joint angle estimation algorithm flowchart.

3.7. Time Complexity Analysis

Based on the flowchart of the joint estimation algorithm, the time complexity analysis is as follows. Assume that a single frame signal consists of M pulses, each with N sampling points, where $N \gg M$. First, a 2D-FFT is performed on the two array signals to identify the peak positions, with a time complexity of $O(MN\log(MN))$. Next, Doppler domain filtering is applied to each array signal, which has a time complexity of $O(MN)$, resulting in a total complexity of $O(MN)$. Then, conjugate cross-correlation is computed, which involves pointwise multiplication and conjugation, with a time complexity of $O(MN)$. Following this, a 2D-FFT is applied to the cross-correlation result, with a time complexity of $O(MN\log(MN))$. In the next step, the peak values in the spectrum are searched, with a time complexity of $O(MN)$, and then a 2D-CZT refinement search is performed based on the peak positions. Assuming the size of the 2D-CZT is $M \times N$, the time complexity is $O(M\log(M) + N\log(N))$. Finally, phase extraction from the peak values is performed, with a time complexity of $O(MN)$. The total time complexity, considering all steps, is dominated by $O(MN\log(MN))$, which is primarily driven by the 2D-FFT operation.

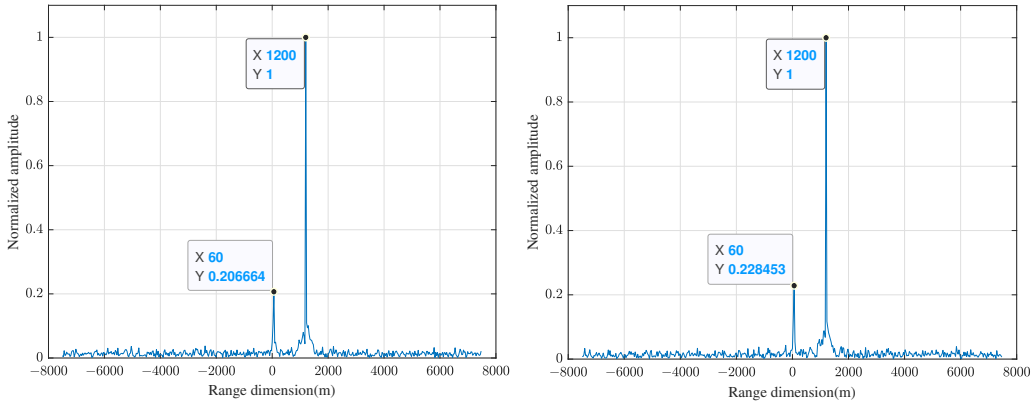
Similarly, it can be concluded that the time complexity of the traditional single-pulse phase comparison method is $N\log(N))$. The increase in time complexity of the proposed joint estimation algorithm, compared to the traditional single-pulse phase comparison method, is primarily due to the utilization of multiple pulses in the computation. The additional complexity arises from operations such as the 2D-FFT, Doppler domain filtering, conjugate cross-correlation, and 2D-CZT refinement, which are essential for leveraging the multi-pulse data to achieve an improved estimation performance.

4. Simulation Results and Discussion

4.1. Static Clutter Removal

In traditional monopulse angle estimation, the use of a single pulse results in incomplete information in the Doppler domain. As a result, whether the target is stationary or moving, corresponding target peaks will appear in the range dimension of the echo signal spectrum. In practical motion target angle estimation scenarios, environments may contain stationary targets with large Radar Cross-Sections (RCSs), such as buildings. These stationary targets manifest as prominent peaks in the spectrum, which can obscure the actual moving targets. Moreover, during conjugate cross-correlation processing of the echo signals from different quadrants, these stationary targets generate spurious peaks that interfere with the precise estimation of moving targets.

As shown in Figure 12, Figure 12a,b display the spectrum of the echo signals from two quadrants. Each spectrum contains two distinct peaks: the right-side peak corresponds to the stationary target while the left-side peak corresponds to the moving target. It is evident that the stationary target peak is much larger than that of the moving target, a result of the larger RCS of stationary targets, such as buildings. Moreover, based solely on these peaks, distinguishing between moving and stationary targets is not possible. The cross-correlation spectrum of the echo signals from the two quadrants is shown in Figure 13. In this spectrum, multiple peaks are observed. At a lower range resolution, stationary targets with large RCSs appear as prominent peaks at zero Doppler frequency, with the highest amplitude. When the target angle is small, such that the wave path difference is minimal, the target peak may be obscured by the stationary target peaks. Furthermore, the presence of multiple peaks complicates the identification of the target peak, thereby hindering precise target angle estimation.



(**a**) (**b**)

Figure 12. Monopulse signals spectrum from each quadrant. (**a**) Monopulse signal spectrum of quadrant A; (**b**) monopulse signal spectrum of quadrant B.

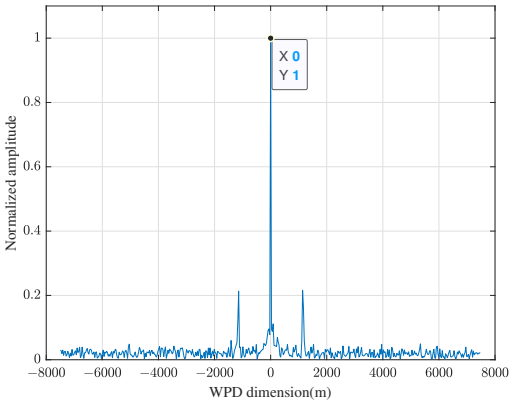
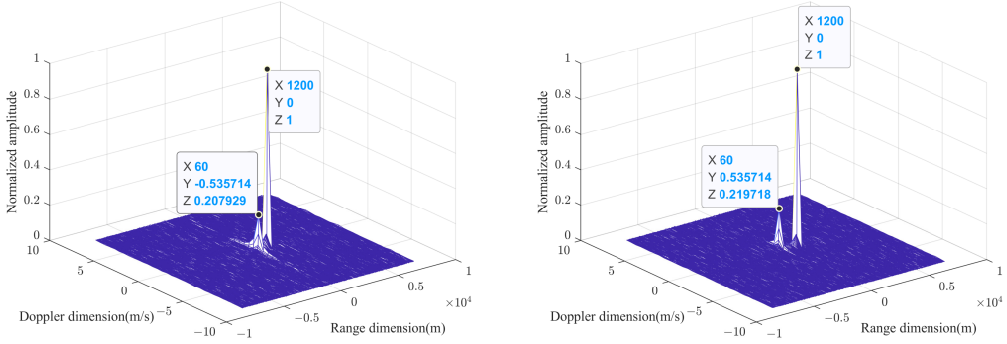


Figure 13. Monopulse cross-correlation signal spectrum.

The multi-pulse angle estimation method based on WPD-ROC AF utilizes the range-Doppler 2D spectrum of echo signals to mitigate the impact of static clutter. The range-Doppler 2D frequency spectra of the two-quadrant echo signals are shown in Figure 14. As observed, both spectra contain a peak at zero Doppler corresponding to stationary targets. However, the actual target peak does not appear at zero Doppler.

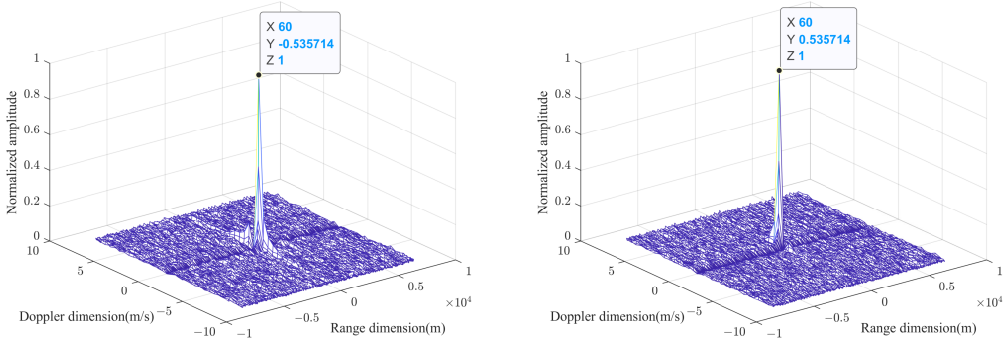


(**a**) (**b**)

Figure 14. The 2D spectrum of the signals from each quadrant. (**a**) The 2D spectrum of quadrant A signal; (**b**) the 2D spectrum of quadrant B signal.

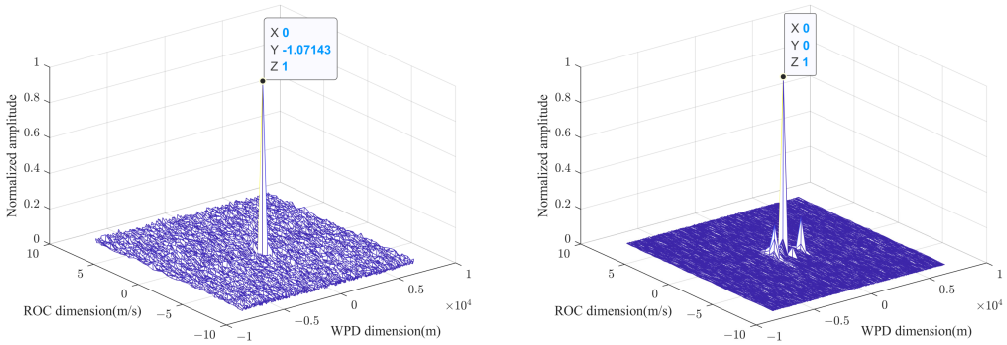
By setting the zero Doppler component to zero, stationary targets can be effectively filtered out. The filtered spectrum is shown in Figure 15, where only the peaks of the

actual moving targets remain. Performing cross-correlation processing on these filtered two-quadrant signals results in the spectrum shown in Figure 16a, which clearly shows a peak corresponding to the moving target, allowing for precise angle estimation based on this peak. In contrast, the original cross-correlation spectrum shown in Figure 16b exhibits multiple peaks, the dominant peak at a zero range rate difference due to its large amplitude, which obscures the other peaks. Comparing the two spectra, it is clear that the proposed method effectively removes the interference from stationary targets, enabling the precise angle estimation of moving targets, even in the presence of static clutter.



(**a**) (**b**)

Figure 15. The 2D spectrum of the echo signals from each quadrant with static clutter removal. (**a**) The 2D spectrum of quadrant A signal with static clutter removal; (**b**) the 2D spectrum of quadrant B signal with static clutter removal.



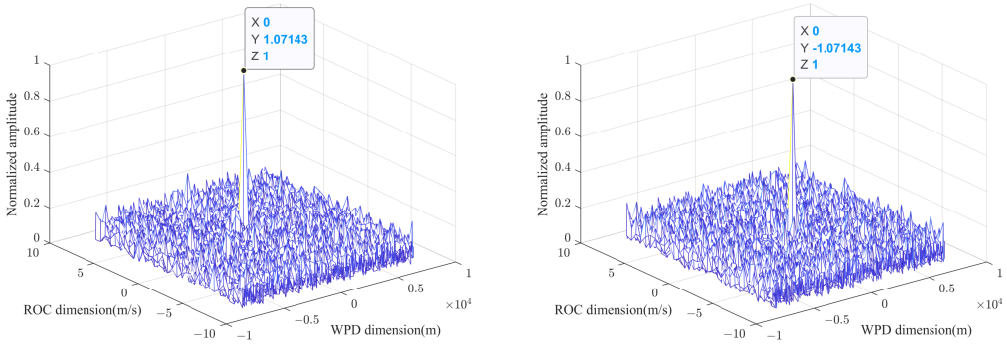
(**a**) (**b**)

Figure 16. The comparison of WPD-ROC AF spectrum with and without static clutter removal. (**a**) The WPD-ROC AF after static clutter removal; (**b**) the WPD-ROC AF without static clutter removal.

4.2. Determination of the Target's Motion Direction

Traditional monopulse angle estimation provides only the target's angle and lacks information about the target's motion trend. In contrast, the WPD-ROC AF is introduced in this study, which offers the target's wave path difference rate, enabling the determination of the target's motion direction based on the sign of this rate. The radar parameters used in the simulations are listed in Table 1. In two rounds of simulations, the target angles are both 0.1°, with wave path difference rates of 1 m/s and -1 m/s, respectively. As shown in Figure 17a, the spectrum peak corresponding to Target 1 is located at 1.07 m/s in the ROC dimension. In Figure 17b, the spectrum peak for Target 2 is located at -1.07 m/s. Due to the limited radar bandwidth, which results in large range resolution, the spectral peaks in the WPD dimension are all located at zero, requiring precise estimation for confirmation.

By determining the sign of the wave path difference rate and combining it with precise angle estimation, the motion direction of the target can be inferred. Therefore, compared to traditional monopulse angle estimation methods, the proposed method provides more detailed information about the target.



(**a**) (**b**)

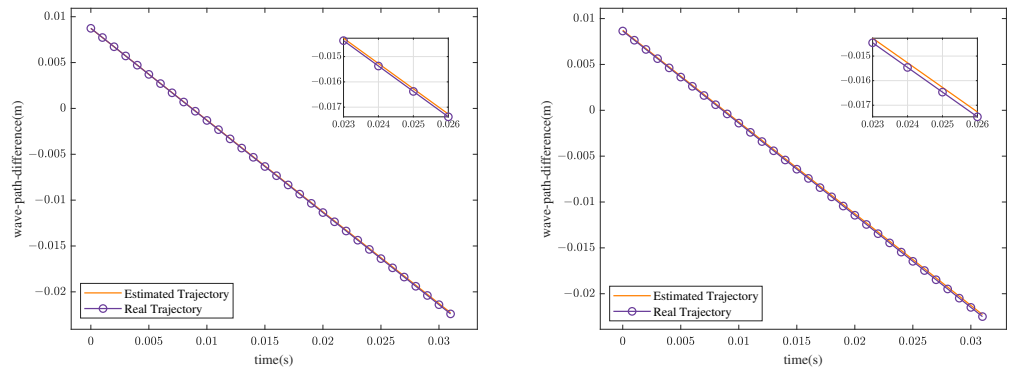
Figure 17. Comparison of WPD-ROC AF spectrum with different target wave path difference rates. (**a**) WPD-ROC AF with the target wave path difference rate of 1 m/s; (**b**) WPD-ROC AF with the target wave path difference rate of -1 m/s.

4.3. The Effect of First-Order Approximation Error

Given the short time duration of a single frame, this study assumes that the rate of WPD remains approximately constant within a single frame, and a first-order model is adopted to represent the temporal evolution of the WPD. To assess whether this first-order approximation causes significant estimation errors, we performed simulations under two conditions.

First, for targets with a constant WPD rate of -1 m/s, the estimated WPD trajectory (estimated using the joint algorithm) closely aligns with the ground-truth WPD variation curve over the frame duration, as illustrated in Figure 18a.

Next, we considered a case where the WPD rate varies over time: the initial WPD rate was set to -1 m/s, and a constant "acceleration" of -1 m/s^2 was applied to the WPD rate. Even with the time-varying WPD rate, the actual WPD curve within a single frame duration remains approximately linear due to the limited observation window. As demonstrated in Figure 18b, the estimation results still exhibit strong agreement with the true target motion characteristics, confirming that the first-order approximation introduces negligible errors under practical frame durations.



(**a**) (**b**)

Figure 18. Simulation of first-order model approximation error impact. (**a**) WPD Variation with Constant Rate; (**b**) WPD Variation with Acceleration.

4.4. Performance Analysis of the Joint Angle Estimation Algorithm

This subsection focuses on validating and analyzing the estimation performance of the joint angle estimation algorithm. The parameters used in the simulation are provided in Table 1.

4.4.1. Estimation Precision Analysis

Figure 19 illustrates the relationship between the Root Mean Square Error (RMSE) of the WPD and the SNR for both the monopulse phase comparison angle estimation method and the proposed joint angle estimation method. It is evident that the proposed method achieves higher estimation precision than the monopulse method, with a lower SNR threshold, thus offering better performance even at low SNR levels. Moreover, as the SNR increases, the WPD estimation precision of the proposed method approaches the corresponding CRLB.

Figure 20 illustrates the relationship between the RMSE of the ROC estimation and the SNR for the proposed method. As observed, as the SNR increases, the ROC estimation precision of the proposed method gradually approaches the CRLB.

For conventional phase comparison monopulse angle estimation methods, the ROC can be indirectly estimated by temporally differencing consecutive WPD measurements derived from angle estimates. The simulation results of this differential estimation approach are shown in Figure 21. The results demonstrate that the RMSE of this differential approach significantly exceeds both our proposed joint estimation method and the theoretical CRLB. This indicates that the cascaded process inevitably amplifies estimation errors while also highlighting the superiority of the proposed method in wave path difference rate estimation.

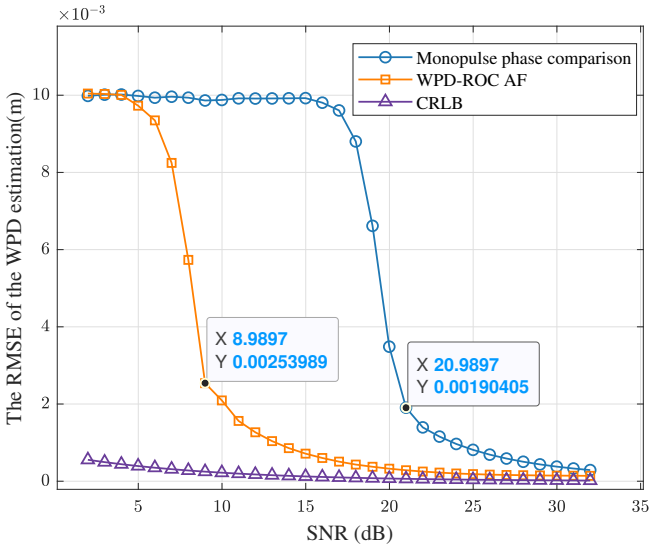


Figure 19. The WPD estimation precision.

Figure 22 shows the relationship between the RMSE of angle estimation and the SNR for both the monopulse phase comparison method and the proposed method. The CRLB for angle estimation is derived from the CRLB of wave path difference, as given in Equation (1).

Additionally, to provide an intuitive understanding of the relationship between estimation accuracy and the SNR, Figure 23 presents the relationship between angle estimation accuracy and the SNR for both methods. This curve is obtained by calculating the ratio of correct angle estimations to the total number of Monte Carlo trials at different SNR levels. Angle estimation accuracy is defined as the deviation between the estimated value and

the true value being no greater than 10%. As observed, the proposed method consistently outperforms the monopulse method, particularly in low-SNR conditions.

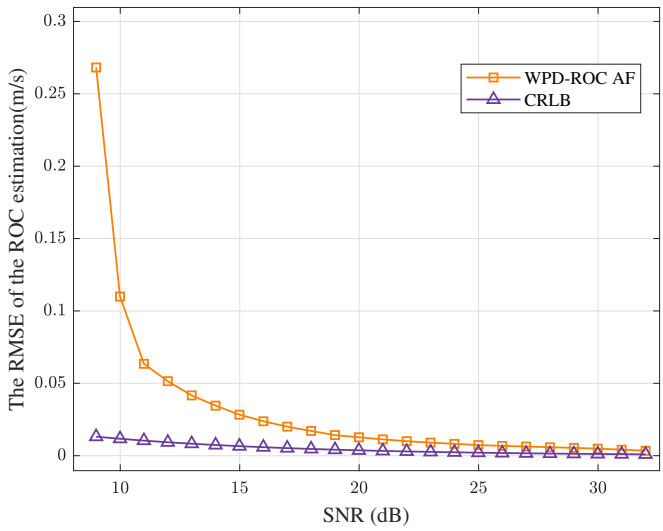


Figure 20. The ROC estimation precision.

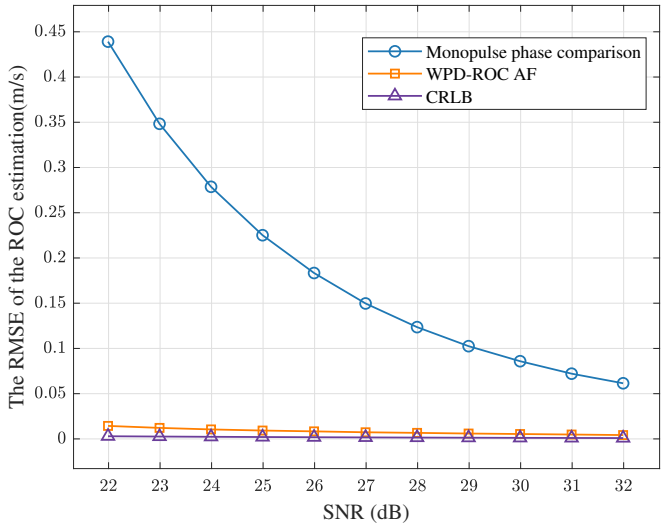


Figure 21. The ROC estimation precision of phase comparison monopulse angle estimation method.

4.4.2. The Effect of Accumulated Pulse Numbers on Estimation Performance

To examine the effect of pulse accumulation on the estimation performance of the proposed joint angle estimation algorithm, Monte Carlo simulations were conducted with pulse counts of 4, 8, 16, and 32 while keeping the target angle and radar parameters constant. The performance comparison is shown in Figures 24 and 25. Figure 24 illustrates the angle estimation precision, demonstrating that as the number of pulses increases, the algorithm's estimation precision improves, and the SNR threshold decreases, resulting in better performance in low-SNR conditions. Figure 25 shows the simulation results of the angle estimation accuracy, indicating that a higher pulse count improves the probability of achieving precise estimations under the same SNR conditions. In conclusion, increasing the pulse count allows for more energy accumulation, which gradually enhances the algorithm's estimation performance.

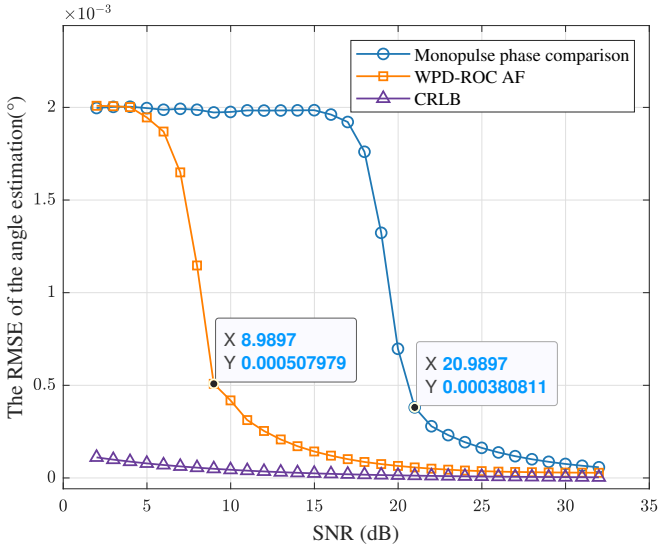


Figure 22. The angle estimation precision.

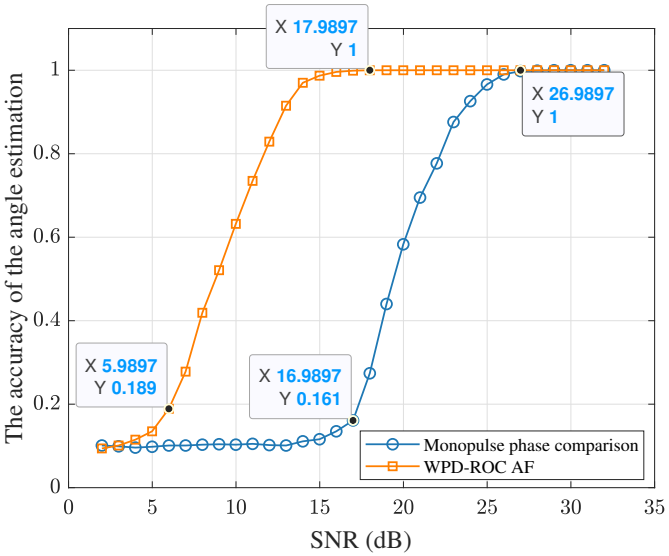


Figure 23. The angle estimation accuracy.

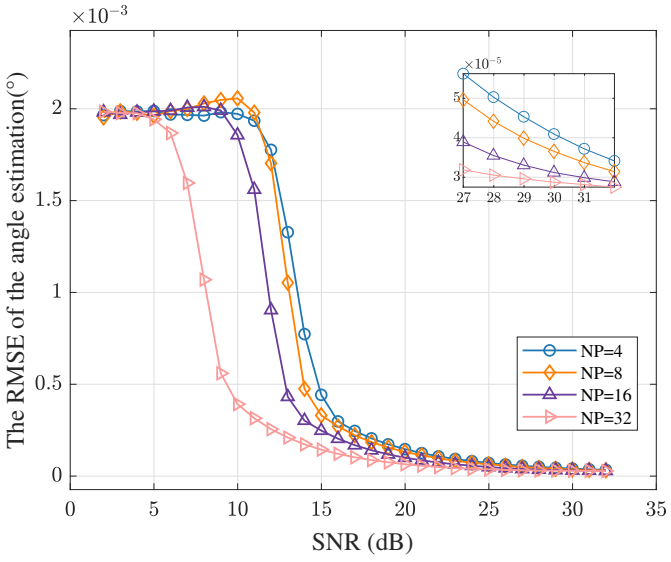


Figure 24. The comparison of angle estimation precision.

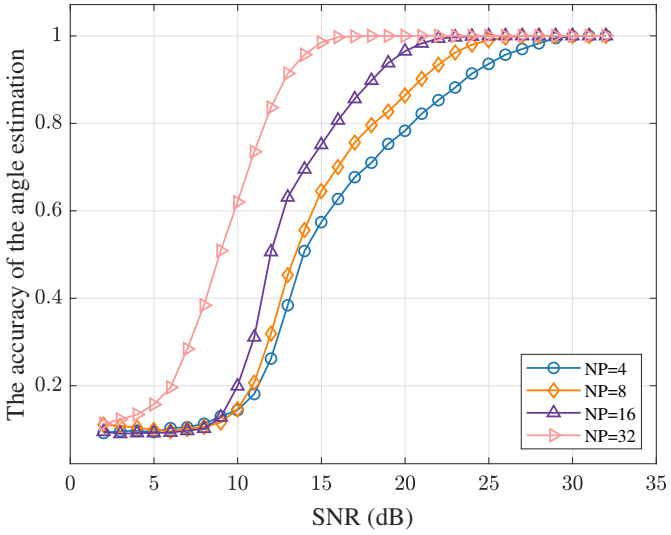


Figure 25. The comparison of angle estimation accuracy.

4.4.3. The Effect of Accumulated Pulse Numbers on Estimation Performance

To examine the effect of quadrant array spacing on the estimation precision of the proposed joint angle estimation algorithm, the array spacings are set to 1 m, 2 m, and 5 m, with other parameters fixed as specified in Table 1. Monte Carlo simulations are conducted under the same conditions for all three setups. The RMSE of the angle estimation results is shown in Figure 26. As observed, increasing the array spacing improves the angle estimation precision while having little effect on the SNR threshold.

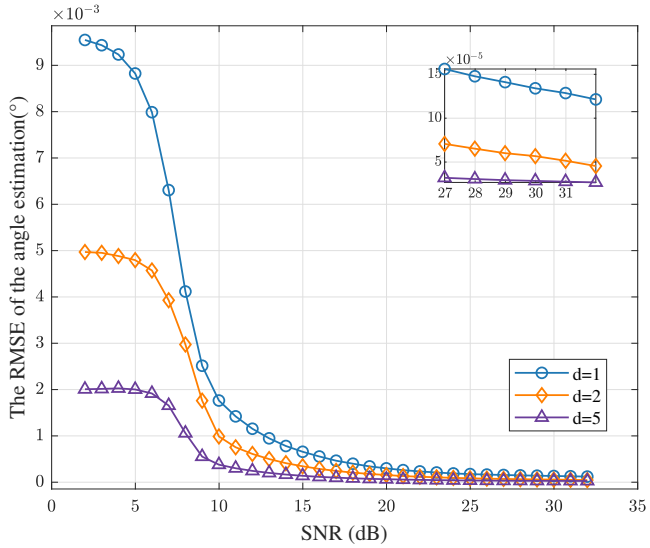


Figure 26. The angle estimation precision under different quadrant array spacings.

In conclusion, this section compares the angle estimation performance of the traditional monopulse phase comparison method with the joint angle estimation method based on the WPD-ROC AF proposed in this study. The results show that the proposed method offers superior angle estimation precision. Furthermore, by overcoming the limitation of the traditional method's poor performance under low-SNR conditions, the proposed approach maintains a robust estimation performance even in low-SNR environments.

5. Conclusions

A joint angle estimation method based on the WPD-ROC AF is presented in this study to address the challenge of target angle estimation under low-SNR conditions. The results show that the proposed method achieves superior angular estimation precision compared to the monopulse phase comparison method, maintaining robust angle estimation performance even under low-SNR environments, which is crucial for remote sensing systems operating in challenging conditions. By utilizing the Doppler information accumulated over multiple pulses, the proposed method effectively separates moving targets from static clutter, enabling precise angle estimation in the presence of static clutter interference. Furthermore, the WPD-ROC AF is capable of determining the target's motion direction, thereby enriching the acquired target motion information. These advancements notwithstanding, two practical challenges warrant deeper exploration to bridge theoretical innovations with real-world implementations: investigating antenna mutual coupling effects in compact array systems and exploring angle estimation under phase mismatch conditions. Addressing these aspects will further enhance the framework's practical applicability across diverse radar architectures.

Author Contributions: Conceptualization, J.X. and M.F.; methodology, validation, and formal analysis, J.X.; writing—original draft preparation, J.X.; writing—review and editing, J.X. and Z.D.; supervision and funding acquisition, Z.D. All authors have read and agreed to the published version of the manuscript.

Funding: The research was supported in part by the Science, Technology, and Innovation Commission of Shenzhen Municipality under Grant JCYJ20210324120002007 and in part by the Science and Technology Planning Project of Key Laboratory of Advanced IntelliSense Technology, Guangdong Science and Technology Department, under Grant 2023B1212060024.

Data Availability Statement: The original contributions presented in this study are included in the article. Further inquiries can be directed to the corresponding author.

Conflicts of Interest: The authors declare no conflicts of interest.

References

1. Liu, F.; Masouros, C.; Petropulu, A.P.; Griffiths, H.; Hanzo, L. Joint radar and communication design: Applications, state-of-the-art, and the road ahead. *IEEE Trans. Commun.* **2020**, *68*, 3834–3862. [CrossRef]
2. Ionescu, L.; Rusu-Casandra, A.; Bira, C.; Tatomirescu, A.; Tramandan, I.; Scagnoli, R.; Istriteanu, D.; Popa, A.E. Development of the Romanian radar sensor for space surveillance and tracking activities. *Sensors* **2022**, *22*, 3546. [CrossRef]
3. Bîră, C.; Ionescu, L.; Rusu-Casandra, A. The Radar Signal Processor of the First Romanian Space Surveillance Radar. *Remote Sens.* **2023**, *15*, 3630. [CrossRef]
4. Misiurewicz, J.; Maslikowūki, Ł.; Gromek, A.; Kurowska, A. MIMO techniques for space surveillance Radar. In Proceedings of the 2019 Signal Processing Symposium (SPSympo), Krakow, Poland, 17–19 September 2019; IEEE: New York, NY, USA, 2019; pp. 199–202.
5. Yan, J.; Pu, W.; Zhou, S.; Liu, H.; Bao, Z. Collaborative detection and power allocation framework for target tracking in multiple radar system. *Inf. Fusion* **2020**, *55*, 173–183. [CrossRef]
6. Blair, W.; Brandt-Pearce, M. Statistical description of monopulse parameters for tracking Rayleigh targets. *IEEE Trans. Aerosp. Electron. Syst.* **1998**, *34*, 597–611. [CrossRef]
7. Nickel, U. Overview of generalized monopulse estimation. *IEEE Aerosp. Electron. Syst. Mag.* **2006**, *21*, 27–56. [CrossRef]
8. Cai, J.; Wang, R.; Yang, H. Angle Expansion Estimation and Correction Based on the Lindeberg–Feller Central Limit Theorem Under Multi-Pulse Integration. *Remote. Sens.* **2024**, *16*, 4535. [CrossRef]
9. Ham, H.W.; Lee, J.H. Improvement of performance analysis of amplitude-comparison monopulse algorithm in the presence of an additive noise. *Electronics* **2021**, *10*, 2649. [CrossRef]
10. Kim, M.; Hong, D.; Park, S. A study on the amplitude comparison monopulse algorithm. *Appl. Sci.* **2020**, *10*, 3966. [CrossRef]
11. An, D.J.; Lee, J.H. Performance analysis of amplitude comparison monopulse direction-of-arrival estimation. *Appl. Sci.* **2020**, *10*, 1246. [CrossRef]

12. Lee, S.H.; Lee, S.J.; Choi, I.O.; Kim, K.T. ICA-based phase-comparison monopulse technique for accurate angle estimation of multiple targets. *IET Radar Sonar Navig.* **2018**, *12*, 323–331. [CrossRef]
13. Islam, S.M.; Yavari, E.; Rahman, A.; Lubecke, V.M.; Boric-Lubecke, O. Multiple subject respiratory pattern recognition and estimation of direction of arrival using phase-comparison monopulse radar. In Proceedings of the 2019 IEEE Radio and Wireless Symposium (RWS), Orlando, FL, USA, 20–23 January 2019; IEEE: New York, NY, USA, 2019; pp. 1–4.
14. Vandana, A.; Jaysaval, V.K.; Reddy, C.B. Enhancement of unambiguous DOA estimation for Phase Comparison Monopulse radar. In Proceedings of the 2015 International Conference on Advances in Computing, Communications and Informatics (ICACCI), Kochi, India, 10–13 August 2015; IEEE: New York, NY, USA, 2015; pp. 1165–1169.
15. Zhang, X.; Li, Y.; Yang, X.; Zheng, L.; Long, T.; Baker, C.J. A novel monopulse technique for adaptive phased array radar. *Sensors* **2017**, *17*, 116. [CrossRef]
16. Han, K.; Hong, S. MIMO monopulse radar for detecting human targets with I/Q curve-length estimations. *IEEE Microw. Wirel. Components Lett.* **2022**, *32*, 214–217. [CrossRef]
17. Blair, W.D.; Brandt-Pearce, M. Unresolved Rayleigh target detection using monopulse measurements. *IEEE Trans. Aerosp. Electron. Syst.* **1998**, *34*, 543–552. [CrossRef]
18. Gini, F.; Greco, M.; Farina, A. Multiple radar targets estimation by exploiting induced amplitude modulation. *IEEE Trans. Aerosp. Electron. Syst.* **2003**, *39*, 1316–1332. [CrossRef]
19. Greco, M.; Gini, F.; Farina, A. Joint use of sum and delta channels for multiple radar target DOA estimation. *IEEE Trans. Aerosp. Electron. Syst.* **2007**, *43*, 1146–1154. [CrossRef]
20. Fu, M.; Gao, C.; Li, Y.; Deng, Z.; Chen, D. Monopulse-radar angle estimation of multiple targets using multiple observations. *IEEE Trans. Aerosp. Electron. Syst.* **2020**, *57*, 968–983. [CrossRef]
21. Mosca, E. Angle estimation in amplitude comparison monopulse systems. *IEEE Trans. Aerosp. Electron. Syst.* **1969**, 205–212. [CrossRef]
22. Zhang, Y.X.; Liu, Q.F.; Hong, R.J.; Pan, P.P.; Deng, Z.M. A novel monopulse angle estimation method for wideband LFM radars. *Sensors* **2016**, *16*, 817. [CrossRef]
23. Chengzeng, C.; Dan, L.; Xiaojian, X.; Yaobing, L. A processing technique for accurate target angle estimation using wideband monopulse radars. *J. Syst. Eng. Electron.* 2024, *early access*. [CrossRef]
24. Han, H.; Xu, X.; Wang, H.; Dai, H. Analysis of cross-polarization jamming for phase comparison monopulse radars. In Proceedings of the 2019 IEEE 2nd International Conference on Electronic Information and Communication Technology (ICEICT), Harbin, China, 20–22 January 2019; IEEE: New York, NY, USA, 2019; pp. 404–407.
25. Van Den Biggelaar, A.; Smolders, A.; Johannsen, U. Method to experimentally verify far-field conditions in a direct far-field measurement setup. In Proceedings of the 2021 Antenna Measurement Techniques Association Symposium (AMTA), Denver, CO, USA, 9–14 October 2022; IEEE: New York, NY, USA, 2021; pp. 1–6.
26. Le Cam, L. Maximum likelihood: An introduction. In *International Statistical Review/Revue Internationale de Statistique*; JSTOR: New York, NY, USA, 1990; pp. 153–171.
27. Voinov, V. *Unbiased Estimators and Their Applications: Univariate Case*; Springer: Berlin/Heidelberg, Germany, 1993; Volume 1.
28. Cavassila, S.; Deval, S.; Huegen, C.; Van Ormondt, D.; Graveron-Demilly, D. Cramér–Rao bounds: An evaluation tool for quantitation. *NMR Biomed. Int. J. Devoted Dev. Appl. Magn. Reson. In Vivo* **2001**, *14*, 278–283. [CrossRef]
29. Song, M.; Lim, J.; Shin, D.J. The velocity and range detection using the 2D-FFT scheme for automotive radars. In Proceedings of the 2014 4th IEEE International Conference on Network Infrastructure and Digital Content, Beijing, China, 19–21 September 2014; IEEE: New York, NY, USA, 2014; pp. 507–510.
30. Rabiner, L.; Schafer, R.W.; Rader, C. The chirp z-transform algorithm. *IEEE Trans. Audio Electroacoust.* **1969**, *17*, 86–92. [CrossRef]
31. Burke, K.; Wagner, L.O. DFT in a nutshell. *Int. J. Quantum Chem.* **2013**, *113*, 96–101. [CrossRef]

Disclaimer/Publisher's Note: The statements, opinions and data contained in all publications are solely those of the individual author(s) and contributor(s) and not of MDPI and/or the editor(s). MDPI and/or the editor(s) disclaim responsibility for any injury to people or property resulting from any ideas, methods, instructions or products referred to in the content.